

Energy-Efficient $W_{100-x}Ta_x/Co\text{-}Fe\text{-}B/MgO$ Spin Hall Nano-Oscillators

Nilamani Behera,¹ Himanshu Fulara^{1,2,*} Lakhan Bainsla¹,¹ Akash Kumar¹,¹
Mohammad Zahedinejad¹,¹ Afshin Houshang,¹ and Johan Åkerman^{1,†}

¹ Physics Department, University of Gothenburg, Gothenburg 412 96, Sweden

² Department of Physics, Indian Institute of Technology Roorkee, Roorkee 247667, India

(Received 16 November 2021; revised 1 April 2022; accepted 1 July 2022; published 5 August 2022)

We investigate a W-Ta alloying route to reduce the auto-oscillation threshold current densities and the power consumption of nanoconstriction based spin Hall nano-oscillators. Using spin-torque ferromagnetic resonance measurements on microbars of $W_{100-x}Ta_x(5\text{ nm})/Co\text{-}Fe\text{-}B(t)/MgO$ stacks with $t = 1.4$, 1.8, and 2.0 nm, we measure a substantial improvement in both the spin-orbit torque efficiency and the spin Hall conductivity. We demonstrate a 34% reduction in auto-oscillation threshold current density, which translates into a 64% reduction in power consumption as compared with pure W-based spin Hall nano-oscillators. Our work demonstrates the promising aspects of W-Ta alloying for the energy-efficient operation of emerging spintronic devices.

DOI: 10.1103/PhysRevApplied.18.024017

I. INTRODUCTION

Current-induced spin-orbit torques (SOTs) [1–3], originating from the spin Hall effect [4–6] in a nonmagnetic heavy metal (HM)/ferromagnet(FM) heterostructure, have recently emerged as a promising energy-efficient route for next-generation ultrafast spintronic devices such as spin Hall nano-oscillators (SHNOs) [7–15], nonvolatile SOT-based magnetic random access memory (MRAM) [16,17], SOT-driven magnonics [18,19], and spin logic devices [20]. The magnetization dynamics in such devices is driven by a pure spin current, which exerts an anti-damping torque on the local magnetization vector of the adjacent FM layer, resulting in magnetization switching in SOT-based MRAM or auto-oscillations in SHNOs.

Nanoconstriction SHNOs [9,21] are currently receiving increasing interest as they demonstrate rich nonlinear magnetodynamics [22–30], can be implemented using a wide range of materials [31–37], and show a great propensity for mutual synchronization [38,39], which leads to orders-of-magnitude-higher signal coherence [39] and allows for oscillator-based neuromorphic computing [39–42] and Ising machines [43,44].

However, a key challenge remains to minimize the switching and auto-oscillation threshold current densities and the associated energy consumption. There has been tremendous effort to enhance the spin Hall angle (θ_{SH}) and the SOT efficiency through various routes such as employing different material combinations [45], incorporating

oxygen [46,47], and dusting the HM surface with Hf [48,49]. Even so, an increase in θ_{SH} is typically achieved at the expense of an equivalent decrease in the longitudinal conductivity (σ_0) leading to high power dissipation during device operation. A better figure of merit is therefore the spin Hall conductivity (SHC): $\sigma_{\text{SH}} = \sigma_0 \theta_{\text{SH}}^{\text{eff}} \hbar / 2e$.

Recent studies have shown that alloying of HMs is a promising route to tune both θ_{SH} and σ_{SH} [50–54]. In 2018, Zhu *et al.* [52] reported highly efficient spin current generation in a $\text{Au}_{0.25}\text{Pt}_{0.75}$ alloy exhibiting a relatively low longitudinal resistivity (ρ_0) of approximately $83\ \mu\Omega\text{ cm}$ and large $\theta_{\text{SH}} \geq 0.58$ in bilayers with Co. Quite recently, Kim *et al.* showed an enhancement of σ_{SH} in W-Ta alloys using spin-torque ferromagnetic resonance (STFMR) measurements [53]. While a reasonably high $\theta_{\text{SH}} = -0.3$ with a relatively low ρ_0 of $100\ \mu\Omega\text{ cm}$ was reported at an 11% Ta concentration, its ultimate effect on σ_{SH} and its potential for reducing the threshold current and the associated energy consumption of SHNOs have yet to be investigated.

Here, we report on an extensive study of W-Ta alloying in $W_{100-x}Ta_x(5\text{ nm})/\text{Co}_{20}\text{Fe}_{60}\text{B}_{20}(t)/\text{MgO}(2\text{ nm})$ nanoconstriction SHNOs with $t = 1.4$, 1.8, and 2.0 nm. W-Ta alloying results in a simultaneous improvement of both $\theta_{\text{SH}}^{\text{eff}}$ and σ_{SH} , which translates into substantial reductions in the threshold current density (J_{th}) and the power consumption. We measure the effective spin Hall angle, $\theta_{\text{SH}}^{\text{eff}} = \theta_{\text{SH}} T_{\text{int}}$, where T_{int} is the interfacial spin transparency between the W-Ta alloy layer and the Co-Fe-B layer. Our measured $\theta_{\text{SH}}^{\text{eff}}$ values are a lower bound of the spin Hall angle in W-Ta alloys [55]. Using STFMR measurements on microbars we first study the magnetodynamical properties to extract $\theta_{\text{SH}}^{\text{eff}}$ and σ_{SH} . $\theta_{\text{SH}}^{\text{eff}}$ first

*himanshu.fulara@ph.iitr.ac.in

†johan.akerman@physics.gu.se

strengthens to an optimum value of -0.61 at 10% Ta, compared with -0.46 for pure β -W, and then weakens to an efficiency of -0.21 as the Ta content is increased to 25%. As the resistivity drops substantially with Ta content, alloying gives rise to a very large approximately 109% increase in σ_{SH} at 18% Ta compared with pure β -W. Both $\theta_{\text{SH}}^{\text{eff}}$ and σ_{SH} scale inversely with the Co-Fe-B thickness, indicating the critical role of transparency of the W-Ta/Co-Fe-B interface [55,56] as expected. Finally, we quantify the alloying effect on the auto-oscillation threshold current densities by fabricating SHNOs of two different constriction widths, 50 and 120 nm. The lowest threshold currents are observed for 12% Ta, with an approximately 34% reduction in auto-oscillation threshold current densities. The reduced threshold current densities translate into a 64% reduced power consumption as compared with pure W-based SHNOs. The trade-off between SOT efficiency, resistivity, and equivalent SHC demonstrates the promising aspects of the W-Ta alloying approach for energy-efficient and CMOS-compatible operation of emerging spintronic devices.

II. EXPERIMENTAL DETAILS

$\text{W}_{100-x}\text{Ta}_x(5 \text{ nm})/\text{Co}_{20}\text{Fe}_{60}\text{B}_{20}(t)/\text{MgO}(2 \text{ nm})$ material stacks, with $t = 1.4$, 1.8, and 2.0 nm, are deposited on highly resistive Si(100) substrates using an AJA Orion-8 magnetron sputtering system, working at a base pressure of 3×10^{-8} Torr, while the argon pressure during sputtering is maintained at 3 mTorr for all layers. A 4-nm SiO_2 capping layer is added to protect the MgO from moisture. The $\text{W}_{100-x}\text{Ta}_x$ alloy films are grown by co-sputtering W and Ta metal targets subjected to dc and rf power, respectively. During deposition, the growth rate of W is kept low at 0.1 Å/s to obtain the desired β -phase with a high spin Hall angle [12,45]. The growth rates of $\text{Co}_{20}\text{Fe}_{60}\text{B}_{20}$, MgO, and SiO_2 layer are maintained at 0.13, 0.06, and 0.08 Å/s, respectively, for good thickness control. The stacks are subsequently annealed at 300 °C for 60 min at the chamber's base pressure to crystallize MgO at the interface as well as Co-Fe-B. Separate individual stacks of pure W, $\text{W}_{100-x}\text{Ta}_x$ alloys, and the Co-Fe-B layers are used for respective resistivity measurements. X-ray diffraction measurements of $\text{W}_{100-x}\text{Ta}_x(5 \text{ nm})/\text{Co}_{20}\text{Fe}_{60}\text{B}_{20}(1.8 \text{ nm})/\text{MgO}(2 \text{ nm})$ thin films are carried out to confirm the phase of W-Ta alloy (see details in Sec. S1 within the Supplemental Material [57]).

To fabricate nanoconstriction SHNOs, the sample stack surface is covered with negative electron resist (HSQ) followed by an exposure to electron beam lithography (RAITH EBL). Nanoconstrictions of 50 and 120 nm are defined in $4 \times 12 \mu\text{m}^2$ mesas. Furthermore, microbars of 6×18 and $6 \times 12 \mu\text{m}^2$ are also designed to characterize the stacks using STFMR measurements. Subsequently, these defined patterns are transferred to the stack

by Ar ion beam etching using an Oxford Ionfab 300 Plus etcher. Later, the negative resist is removed, and optical lift-off lithography is carried out to define ground-ground coplanar waveguides (CPWs) of a thick Cu(800 nm)/Pt(20 nm) bilayer. To ensure a good electrical contact between the CPWs and the SHNOs, the MgO/ SiO_2 layers are removed in the CPW-defined area by substrate plasma cleaning at a rf power of 40 W in the AJA Orion-8 sputtering chamber immediately before Cu/Pt deposition.

The spin transport measurements on the microbar devices are carried out using a room-temperature STFMR setup with a fixed in-plane angle, $\phi = 30^\circ$, to estimate the SOT efficiencies and other magnetodynamical parameters. Figure 1(a) schematically illustrates the STFMR measurement details on the patterned 6- μm -width bars of all $\text{W}_{100-x}\text{Ta}_x(5 \text{ nm})/\text{Co-Fe-B}(1.4\text{--}2 \text{ nm})/\text{MgO}(2 \text{ nm})$ stacks. The microwave current, I_{rf} , is modulated at 98.76 Hz, and injected into the microbars through a high-frequency bias tee, producing spin-orbit torques and Oersted field in the presence of out-of-plane (OOP) magnetic field. The Oersted field generates an OOP torque on the Co-Fe-B magnetization (τ_{Oe}) and additional fieldlike torque (τ_{FL}) and dampinglike torque (τ_{DL}) are induced due to exchange interaction of the transverse spin current density with the magnetization in the Co-Fe-B layer [58]. These torques govern the magnetization dynamics in the Co-Fe-B layer, which results in an oscillatory change in the resistance of the device due to anisotropic magnetoresistance (AMR) and spin Hall magnetoresistance of the Co-Fe-B layer. The oscillating resistance mixes with I_{rf} and produces a dc voltage (V_{mix}) across the microbar, which is detected on the modulating frequency using a lock-in amplifier.

All magnetization auto-oscillation measurements are performed using a custom-built probe station with the sample mounted at a fixed in-plane angle on an OOP rotatable sample holder lying between the pole pieces of an electromagnet generating a uniform magnetic field. Figure 1(b) schematically shows the experimental setup for auto-oscillation measurements of a SHNO device of width of 120 nm. Here, a positive direct current is fed to the SHNO device through the dc port of the high-frequency bias tee under a fixed OOP magnetic field and the resulting auto-oscillation signal is first amplified by a low-noise amplifier of gain 72 dB and thereafter recorded using a Rohde & Schwarz (10 Hz to 40 GHz) spectrum analyzer with a low-resolution bandwidth of 300 kHz.

III. RESULTS AND DISCUSSION

Sheet resistance measurements are carried out on $\text{W}_{100-x}\text{Ta}_x(5 \text{ nm})$ alloy thin films to determine their resistivity versus Ta concentration. Figure 1(c), showing a plot of ρ versus Ta concentration, reveals that the resistivity starts out at $300 \mu\Omega \text{ cm}$, which is the typical resistivity for A15 type of materials [45,59], and then exhibits a steep

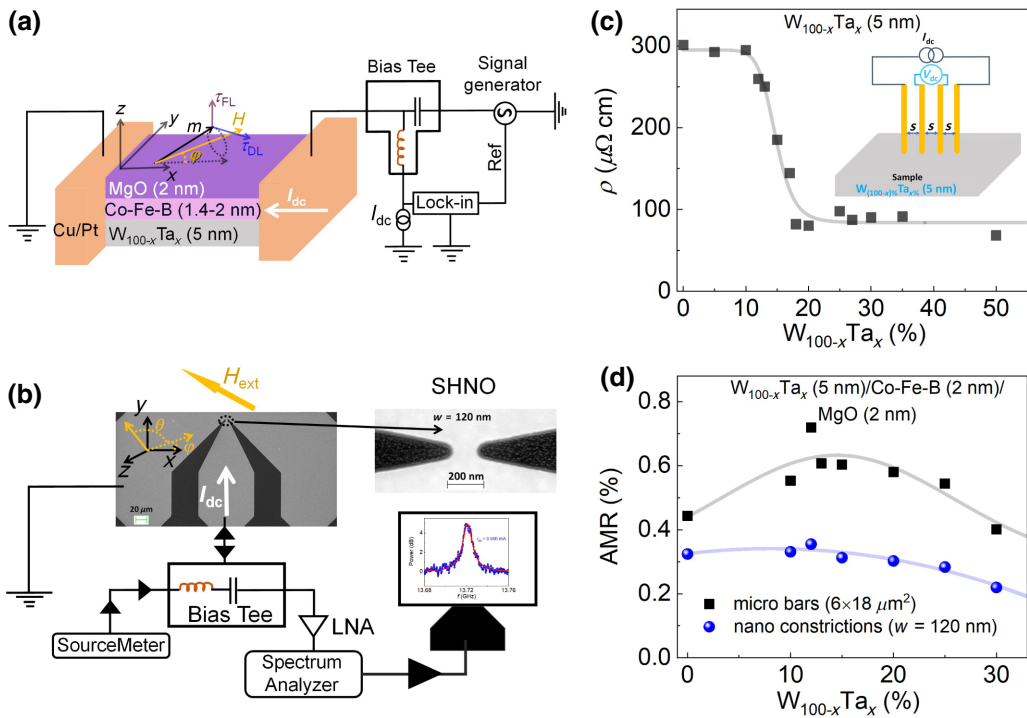


FIG. 1. Device schematic, resistivity, and magnetoresistance. (a) Schematic of STFMR measurement setup. (b) Schematic of auto-oscillation measurement setup along with scanning electron micrograph image of a SHNO with 120-nm nanoconstriction width. (c) Variation of resistivity of W-Ta alloy thin films as a function of Ta composition. Solid line shows the average behavior of resistivity variation with W-Ta alloy composition. (d) AMR measured as a function of different W-Ta alloy composition on microbars (black squares) and 120-nm nanoconstrictions (blue dots). Solid line shows the average behavior of magnetoresistance variation with W-Ta alloy composition.

drop, between 10% and 18% Ta, to about $90 \mu\Omega \text{ cm}$ for all higher concentrations, i.e. a difference of greater than 3 times. Figure 1(d) shows the W_{100-x}Ta_x composition-dependent AMR behavior of $(6 \times 18)\text{-}\mu\text{m}^2$ microbars and 120-nm nanoconstrictions. The AMR shows a maximum at 12% Ta as compared with pure W and then trends downward with further increase of Ta concentration.

STFMR measurements of all W_{100-x}Ta_x(5 nm)/Co-Fe-B(1.4–2 nm)/MgO(2 nm) stacks are carried out to estimate θ_{SH}^{eff}, i.e., charge to spin current conversion efficiency. The observed STFMR spectra (see Fig. S2 within the Supplemental Material [57]) are fitted with a sum of symmetric [$F_S(H)$] and anti-symmetric [$F_A(H)$] Lorentzians [46,60] as $V_{\text{mix}} = V_0[SF_S(H) + AF_A(H)]$, where V_0 is the amplitude of the mixing voltage and S and A are the symmetric and anti-symmetric Lorentzian weight factors, accounting for dampinglike and fieldlike torques, respectively. The resonance field (H_r) and linewidth (ΔH) are extracted and the effective magnetization, $\mu_0 M_{\text{eff}}$, is determined from fits of f vs H_r to the Kittel equation, $f = (\gamma/2\pi)\mu_0\sqrt{(H_r + H_k)(H_r + H_k + M_{\text{eff}})}$, by assuming constant gyromagnetic ratio values for all concentrations of W_{100-x}Ta_x but different values for different Co-Fe-B thicknesses: $\gamma/2\pi = 29.4, 30.4$, and 30.5 GHz/T

for 1.4, 1.8, and 2 nm. The Gilbert damping (α) is extracted from ΔH vs f using $\Delta H = \Delta H_0 + (2\pi\alpha f)/\gamma$. The Ta concentration-dependent α and $\mu_0 M_{\text{eff}}$ are plotted in Fig. S3 within the Supplemental Material [57].

The effective spin Hall angle, $\theta_{\text{SH}}^{\text{eff}}$, is then determined from the dc-dependent STFMR linewidth (ΔH vs I_{dc}) analysis [45,46,60]. The inset of Fig. 2(a) shows a plot of ΔH^* vs I_{dc} , where $\Delta H^* = [\Delta H(I_{\text{dc}}) - \Delta H(I_{\text{dc}} = 0)]$ varies linearly with I_{dc} with a slope $\delta\Delta H/\delta(I_{\text{dc}})$ indicating the strength of the SOT from which we extract [60]

$$\theta_{\text{SH}}^{\text{eff}} = \frac{2e}{\hbar} \frac{(H + 0.5M_{\text{eff}})\mu_0 M_s t_{\text{FM}}}{\sin\phi} \frac{\gamma}{2\pi f} \frac{\delta\Delta H}{\delta(I_{\text{dc},\text{HM}})} A_c, \quad (1)$$

with ϕ the azimuthal angle between I_{dc} and $\mu_0 H$, $\mu_0 M_{\text{eff}}$ the effective magnetization, $M_s = 9.31 \times 10^5 \text{ (A/m)}$ the saturation magnetization of the Co-Fe-B layer [12], \hbar and e the reduced Planck's constant and elementary charge, t_{FM} the thickness of FM layer (Co-Fe-B), and A_c the cross-sectional area of the microbars. The current in the HM layer, $I_{\text{dc},\text{HM}}$, is calculated using a parallel resistor model from the measured resistivity of individual FM and HM layers. For the estimation of $\theta_{\text{SH}}^{\text{eff}}$, the resistivity values as shown in Fig. 1(b) are used for W_{100-x}Ta_x(5 nm)

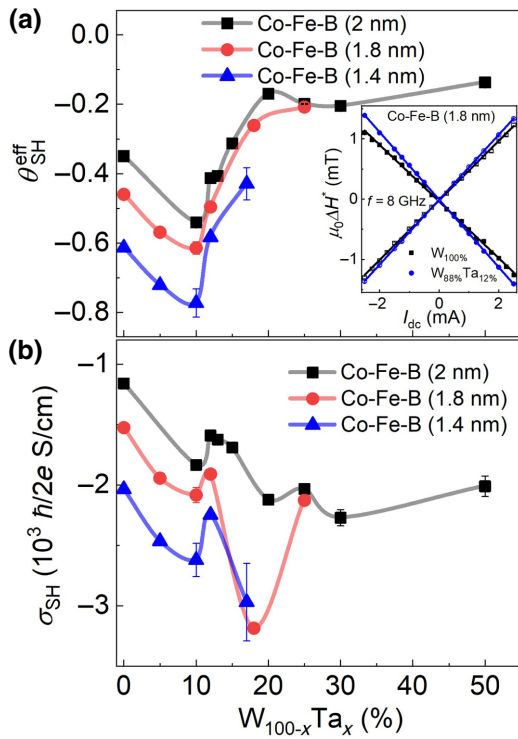


FIG. 2. STFMR measurements performed on $W_{100-x}Ta_x(5\text{ nm})/Co_{20}Fe_{60}B_{20}(t_{Co-Fe-B} = 1.4, 1.8 \text{ and } 2\text{ nm})/\text{MgO}(2\text{ nm})$ microbars. (a) Dependence of effective spin Hall angle (θ_{SH}^{eff}) on W-Ta alloy composition for three different Co-Fe-B thicknesses exhibiting similar behavior. Solid line shows the average behavior. Inset shows linewidth dependence on dc to estimate SOT efficiency. (close symbols for positive and open symbols for negative direction of applied magnetic field) (b) Variation of spin Hall conductivity (σ_{SH}) as a function of W-Ta alloy composition shown for three different Co-Fe-B thicknesses.

alloys and the resistivity value of Co-Fe-B, $64 \mu\Omega \text{ cm}$, is determined from Co-Fe-B thickness-dependent sheet conductance behavior (see Fig. S4 within the Supplemental Material [57]) [61,62]. We further extract the dampinglike torque efficiencies (ξ_{DLT}) [46] and fieldlike torque efficiencies (ξ_{FLT}) [63] as functions of Ta composition and Co-Fe-B thickness (see Fig. S5 within the Supplemental Material [57]).

As expected, we first observe a monotonic strengthening of θ_{SH}^{eff} from -0.35 to -0.62 with decreasing Co-Fe-B layer thickness, highlighting the interfacial nature of SOT. Then, for all three different Co-Fe-B layer thicknesses, the behavior of θ_{SH}^{eff} remains qualitatively similar with W-Ta alloy composition, first strengthening linearly with Ta content up to 10% Ta, then abruptly changing character to rapidly weakening with Ta content until leveling off above 20% Ta. This behavior is quite consistent with the resistivity dependence on W-Ta composition, as shown in Fig. 1(c). As shown in Fig. 2(a), θ_{SH}^{eff} decreases in the region ($x = 10\%$ to 20%) where the resistivity shows a steep

drop, which is possibly due to the formation of a mixed ($\alpha + \beta$) W phase due to increased Ta alloying.

We also estimate the spin Hall conductivity using the relation $\theta_{SH}^{eff} = (2e/\hbar)(\sigma_{SH}/\sigma_0)$ [62]. Figure 2(b) shows the dependence of σ_{SH} on W-Ta alloy composition, indicating a qualitatively similar behavior for all Co-Fe-B thicknesses. We observe the strongest σ_{SH} of $-3186(\hbar/2e) \text{ (S/cm)}$ at 18% Ta, which is an approximately 109% increase compared with pure W, higher than earlier reported values [53,54], but still lower than the theoretically predicted ultimate values [51,64]. The improved σ_{SH} values observed in our work indicate the combined effect of reduced Co-Fe-B layer thickness and optimum W-Ta alloying.

Next, we quantify how the observed improvements in θ_{SH}^{eff} and σ_{SH} can eventually lead to energy savings in practical devices. We first perform auto-oscillation measurements on nanoconstriction SHNOs fabricated from identical $W_{100-x}Ta_x(5\text{ nm})/Co-Fe-B(t = 1.4\text{--}2\text{ nm})/\text{MgO}(2\text{ nm})$ stacks. Figures 3(a)–3(d) show the current-dependent power spectral density (PSD) plots, measured under a fixed OOP field of 0.3 T , for 120-nm - and 50-nm -wide SHNOs. Except for Fig. 3(b), all f versus current data look mainly monotonic. The nonmonotonic current dependence of the auto-oscillation frequency is typical for these SHNOs due to localized auto-oscillations governed by negative nonlinearity in the constriction region [23]. The localization can be fully mitigated by inducing strong perpendicular magnetic anisotropy in the ferromagnetic layer, resulting in the excitation of truly propagating spin-wave auto-oscillations in the constriction region [29,30]. Notably, as shown in Fig. 3(a), we observe a large reduction of threshold current from approximately $260 \mu\text{A}$ for pure W to approximately $160 \mu\text{A}$ for $W_{88}Ta_{12}$, clearly demonstrating the direct benefit of improved SOT efficiency and spin Hall conductivity. This general trend is observed in other nanoconstriction widths as shown in Figs. 3(c) and 3(d), where a 50-nm nanoconstriction shows a similar large drop in the threshold current, reaching the sub- $100\text{-}\mu\text{A}$ regime. Note that we also observe a qualitatively different current tunability of frequency as we measure auto-oscillations for smaller constriction widths. This is because the effective demagnetization field produced by the constriction edges for narrower constriction width is quite substantial and, therefore, the nonlinearity remains positive at all operational currents leading to a blue-shifted frequency behavior in the entire current range [14,21].

In Fig. 4(a), we summarize the behavior of threshold current densities, $J_{th,W-Ta}$, extracted from auto-oscillation measurements for the 120-nm -width SHNOs using the method given in Ref. [65] and in the Supplemental Material (S6) [57]. $J_{th,W-Ta}$ initially decreases with increasing Ta composition (0% to 12%), and after that increases with higher Ta compositions. The observed trend is qualitatively consistent for different Co-Fe-B thicknesses, as

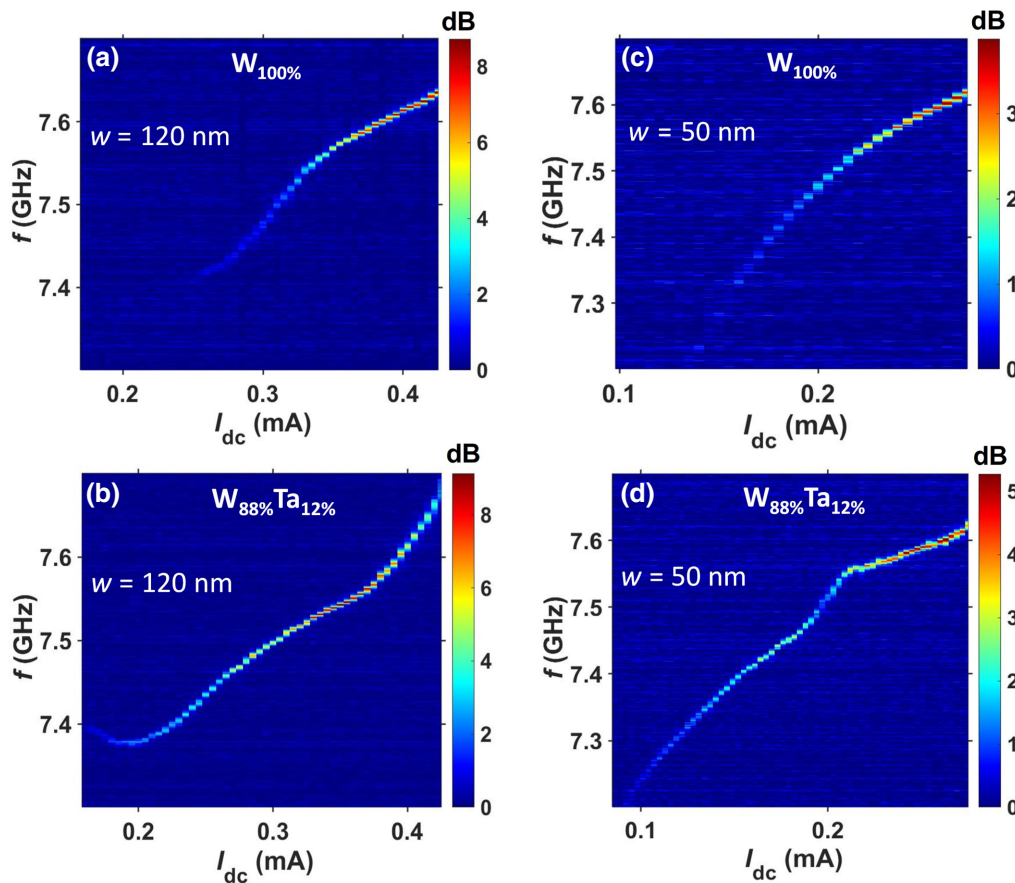
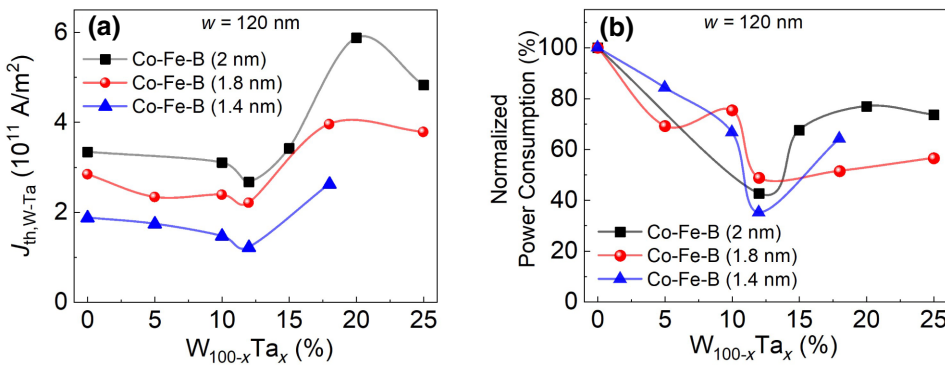


FIG. 3. PSD plots of the auto-oscillations versus current showing a consistent drop in threshold currents of W-Ta alloy-based SHNOs comprising Co-Fe-B of thickness $t_{\text{Co-Fe-B}} = 1.4 \text{ nm}$, measured at out-of-plane magnetic field $\mu_0 H = 0.3 \text{ T}$, $\theta = 60^\circ$, $\phi = 22^\circ$.

shown in Fig. 4(a). We observe a considerable 34% reduction in $J_{\text{th},W\text{-Ta}}$ as compared with pure W. Further, we estimate the effective power consumption to drive W-Ta based SHNOs using $P = (I_{\text{th}})^2 R$, where R is the resistance of the SHNO, and normalized by the power consumption in pure W-based SHNOs. Figure 4(b) shows the comparison of normalized power consumption for different Co-Fe-B thicknesses, showing a trend of power consumption similar to that of Fig. 4(a). The normalized power consumption shows a minimum value of about 36% at 12% Ta for 1.4-nm Co-Fe-B thickness, indicating an overall large 64% reduction in effective power consumption as a result of W-Ta alloying.



Note that we obtain the most reduction in power consumption at 12% Ta concentration with values of $\sigma_{\text{SH}} = -2247(\hbar/2e) \text{ (S/cm)}$ and $\theta_{\text{SH}}^{\text{eff}} = -0.58$, despite a minor change in resistivity from 300 to $260 \mu\Omega \text{ cm}$. We argue that the substituted Ta atoms in the cage of W atoms give rise to a minimal distortion of the A15 structure, which can be seen as an apparent increase in $\theta_{\text{SH}}^{\text{eff}}$ value at 12% Ta concentration. However, with increased Ta alloying, W-Ta resistivity shows a steep drop and $\theta_{\text{SH}}^{\text{eff}}$ follows a similar trend. We believe that increased Ta alloying results in structural changes from β -W phase to $(\alpha + \beta)$ -W-Ta phase. Our results evidence that controlled alloying of W with Ta is critical to minimize power

FIG. 4. (a) Variation of threshold current density in W_{100-x}Ta_x layer as a function of W-Ta alloy composition, extracted for different Co-Fe-B thicknesses. (b) Dependence of normalized threshold power consumption in a 120-nm SHNO device on W-Ta alloy composition, showing a large 64% drop in power consumption.

consumption in SHNOs and we identify this range as $x = 10\%$ to 20%.

IV. CONCLUSION

We demonstrate a W-Ta alloying route to minimize the auto-oscillation threshold current densities and the power consumption in nanoconstriction-based SHNOs. The controlled alloying of W with Ta results in a considerable drop in the resistivity, which not only increases the SOT efficiency but also significantly enhances the spin Hall conductivity of the W-Ta layer. As a direct consequence, we observe a large 34% drop in threshold current density of SHNOs. The estimated effective power consumption further drops by 64%, indicating the tremendous potential of the alloying approach over other methods for reducing the energy consumption in emerging spintronic devices. Further reduction of the constriction width to 20 nm and below should push SHNO operation into the regime of tens of microamps. Our experimental results for SHNO devices not only benefit oscillator-based neuromorphic computing in terms of power consumption but also make the alloy route attractive for other spintronic applications.

ACKNOWLEDGMENTS

This work is partially supported by the Horizon 2020 research and innovation program No. 835068 “TOPSPIN.” This work is also partially supported by the Swedish Research Council (VR Grant No. 2016-05980) and the Knut and Alice Wallenberg Foundation.

Magnetic nano-oscillator driven by pure spin current, *Nat. Mater.* **11**, 1028 (2012).

- [8] L. Liu, C.-F. Pai, D. C. Ralph, and R. A. Buhrman, Magnetic Oscillations Driven by the Spin Hall Effect in 3-Terminal Magnetic Tunnel Junction Devices, *Phys. Rev. Lett.* **109**, 186602 (2012).
- [9] V. E. Demidov, S. Urazhdin, A. Zholud, A. V. Sadovnikov, and S. O. Demokritov, Nanoconstriction-based spin-Hall nano-oscillator, *Appl. Phys. Lett.* **105**, 172410 (2014).
- [10] M. Ranjbar, P. Dürrenfeld, M. Haidar, E. Iacocca, M. Balinskiy, T. Q. Le, M. Fazlali, A. Houshang, A. A. Awad, R. K. Dumas, and J. Åkerman, CoFeB-based spin Hall nano-oscillators, *IEEE Magn. Lett.* **5**, 3000504 (2014).
- [11] T. Chen, R. K. Dumas, A. Eklund, P. K. Muduli, A. Houshang, A. A. Awad, Dürrenfeld, B. G. Malm, A. Rusu, and J. Åkerman, Spin-torque and spin-hall nano-oscillators, *P. IEEE* **104**, 1919 (2016).
- [12] M. Zahedinejad, H. Mazraati, H. Fulara, J. Yue, S. Jiang, A. A. Awad, and J. Åkerman, CMOS compatible W/CoFeB/MgO spin Hall nano-oscillators with wide frequency tunability, *Appl. Phys. Lett.* **112**, 132404 (2018).
- [13] M. Haidar, A. A. Awad, M. Dvornik, R. Khymyn, A. Houshang, and J. Åkerman, A single layer spin-orbit torque nano-oscillator, *Nat. Commun.* **10**, 2362 (2019).
- [14] P. Dürrenfeld, A. A. Awad, A. Houshang, R. K. Dumas, and J. Åkerman, A 20 nm spin Hall nano-oscillator, *Nanoscale* **9**, 1285 (2017).
- [15] Z. Duan, A. Smith, L. Yang, B. Youngblood, J. Lindner, V. E. Demidov, S. O. Demokritov, and I. N. Krivorotov, Nanowire spin torque oscillator driven by spin orbit torques, *Nat. Commun.* **5**, 5616 (2014).
- [16] L. Liu, C.-F. Pai, Y. Li, H. W. Tseng, D. C. Ralph, and R. A. Buhrman, Spin-torque switching with the giant spin Hall effect of tantalum, *Science* **336**, 555 (2012).
- [17] I. M. Miron, K. Garello, G. Gaudin, P.-J. Zermatten, M. V. Costache, S. Auffret, S. Bandiera, B. Rodmacq, A. Schuhl, and P. Gambardella, Perpendicular switching of a single ferromagnetic layer induced by in-plane current injection, *Nature* **476**, 189 (2011).
- [18] X. Xing, P. W. T. Pong, J. Åkerman, and Y. Zhou, Paving Spin-Wave Fibers in Magnonic Nanocircuits Using Spin-Orbit Torque, *Phys. Rev. Appl.* **7**, 054016 (2017).
- [19] V. E. Demidov, S. Urazhdin, A. Anane, V. Cros, and S. O. Demokritov, Spin-orbit-torque magnonics, *J. Appl. Phys.* **127**, 170901 (2020).
- [20] B. Dieny, *et al.*, Opportunities and challenges for spintronics in the microelectronics industry, *Nat. Electron.* **3**, 446 (2020).
- [21] A. A. Awad, A. Houshang, M. Zahedinejad, R. Khymyn, and J. Åkerman, Width dependent auto-oscillating properties of constriction based spin Hall nano-oscillators, *Appl. Phys. Lett.* **116**, 232401 (2020).
- [22] M. Zahedinejad, A. A. Awad, P. Dürrenfeld, A. Houshang, Y. Yin, P. K. Muduli, and J. Åkerman, Current modulation of nanoconstriction spin-hall nano-oscillators, *IEEE Magn. Lett.* **8**, 1 (2017).
- [23] M. Dvornik, A. A. Awad, and J. Åkerman, Origin of Magnetization Auto-Oscillations in Constriction-Based Spin Hall Nano-Oscillators, *Phys. Rev. Appl.* **9**, 014017 (2018).
- [24] T. M. Spicer, P. S. Keatley, T. H. J. Loughran, M. Dvornik, A. A. Awad, P. Dürrenfeld, A. Houshang, M. Ranjbar,

- J. Åkerman, V. V. Kruglyak, and R. J. Hicken, Spatial mapping of torques within a spin Hall nano-oscillator, *Phys. Rev. B* **98**, 214438 (2018).
- [25] H. Mazraati, S. R. Etesami, S. A. H. Banuazizi, S. Chung, A. Houshang, A. A. Awad, M. Dvornik, and J. Åkerman, Auto-oscillating Spin-Wave Modes of Constriction-Based Spin Hall Nano-oscillators in Weak In-Plane Fields, *Phys. Rev. Appl.* **10**, 054017 (2018).
- [26] T. Hache, T. Weinhold, K. Schultheiss, J. Stigloher, F. Vilsmeier, C. Back, S. S. P. K. Arekapudi, O. Hellwig, J. Fassbender, and H. Schultheiss, Combined frequency and time domain measurements on injection-locked, constriction-based spin Hall nano-oscillators, *Appl. Phys. Lett.* **114**, 102403 (2019).
- [27] A. Smith, K. Sobotkiewich, A. Khan, E. A. Montoya, L. Yang, Z. Duan, T. Schneider, K. Lenz, J. Lindner, K. An, X. Li, and I. N. Krivorotov, Dimensional crossover in spin Hall oscillators, *Phys. Rev. B* **102**, 054422 (2020).
- [28] B. Divinskiy, V. E. Demidov, S. Urazhdin, R. Freeman, A. B. Rinkevich, and S. O. Demokritov, Excitation and amplification of spin waves by spin-orbit torque, *Adv. Mater.* **30**, 1802837 (2017).
- [29] H. Fulara, M. Zahedinejad, R. Khymyn, A. A. Awad, S. Muralidhar, M. Dvornik, and J. Åkerman, Spin-orbit torque–driven propagating spin waves, *Sci. Adv.* **5**, eaax8467 (2019).
- [30] H. Fulara, M. Zahedinejad, R. Khymyn, M. Dvornik, S. Fukami, S. Kanai, H. Ohno, and J. Åkerman, Giant voltage-controlled modulation of spin Hall nano-oscillator damping, *Nat. Commun.* **11**, 4006 (2020).
- [31] H. Mazraati, S. Chung, A. Houshang, M. Dvornik, L. Piazza, F. Qeivanaj, S. Jiang, T. Q. Le, J. Weissenrieder, and J. Åkerman, Low operational current spin Hall nano-oscillators based on NiFe/W bilayers, *Appl. Phys. Lett.* **109**, 242402 (2016).
- [32] M. Evelt, C. Safranski, M. Aldosary, V. E. Demidov, I. Barsukov, A. P. Nosov, A. B. Rinkevich, K. Sobotkiewich, X. Li, J. Shi, I. N. Krivorotov, and S. O. Demokritov, Spin Hall-induced auto-oscillations in ultrathin YIG grown on Pt, *Sci. Rep.* **8**, 1269 (2018).
- [33] T. Hache, Y. Li, T. Weinhold, B. Scheumann, F. J. T. Gonçalves, O. Hellwig, J. Fassbender, and H. Schultheiss, Bipolar spin Hall nano-oscillators, *Appl. Phys. Lett.* **116**, 192405 (2020).
- [34] M. Haidar, H. Mazraati, P. Dürrenfeld, H. Fulara, M. Ranjbar, and J. Åkerman, Compositional effect on auto-oscillation behavior of Ni_{100-x}Fe_x/Pt spin Hall nano-oscillators, *Appl. Phys. Lett.* **118**, 012406 (2021).
- [35] N. Sato, K. Schultheiss, L. Körber, N. Puwenberg, T. Mühl, A. A. Awad, S. S. P. K. Arekapudi, O. Hellwig, J. Fassbender, and H. Schultheiss, Domain Wall Based Spin-Hall Nano-Oscillators, *Phys. Rev. Lett.* **123**, 057204 (2019).
- [36] C. Safranski, E. A. Montoya, and I. N. Krivorotov, Spin-orbit torque driven by a planar Hall current, *Nat. Nanotechnol.* **14**, 27 (2019).
- [37] J.-R. Chen, A. Smith, E. A. Montoya, J. G. Lu, and I. N. Krivorotov, Spin-orbit torque nano-oscillator with giant magnetoresistance readout, *Commun. Phys.* **3**, 187 (2020).
- [38] A. A. Awad, P. Dürrenfeld, A. Houshang, M. Dvornik, E. Iacocca, R. K. Dumas, and J. Åkerman, Long-range mutual synchronization of spin Hall nano-oscillators, *Nat. Phys.* **13**, 292 (2017).
- [39] M. Zahedinejad, A. A. Awad, S. Muralidhar, R. Khymyn, H. Fulara, H. Mazraati, M. Dvornik, and J. Åkerman, Two-dimensional mutually synchronized spin Hall nano-oscillator arrays for neuromorphic computing, *Nat. Nanotechnol.* **15**, 47 (2020).
- [40] U. Singh, N. Garg, S. Kumar, P. K. Muduli, and D. Bhowmik, Learning of classification tasks with an array of uniform-mode spin Hall nano-oscillators, *AIP Adv.* **11**, 045117 (2021).
- [41] M. Zahedinejad, H. Fulara, R. Khymyn, A. Houshang, M. Dvornik, S. Fukami, S. Kanai, H. Ohno, and J. Åkerman, Memristive control of mutual spin Hall nano-oscillator synchronization for neuromorphic computing, *Nat. Mater.* **21**, 81 (2022).
- [42] N. Garg, S. V. H. Bhotla, P. K. Muduli, and D. Bhowmik, Kuramoto-model-based data classification using the synchronization dynamics of uniform-mode spin Hall nano-oscillators, *Neuromorph. Comput. Eng.* **1**, 024005 (2021).
- [43] D. I. Albertsson, M. Zahedinejad, A. Houshang, R. Khymyn, J. Åkerman, and A. Rusu, Ultrafast Ising Machines using spin torque nano-oscillators, *Appl. Phys. Lett.* **118**, 112404 (2021).
- [44] A. Houshang, M. Zahedinejad, S. Muralidhar, R. Khymyn, M. Rajabali, H. Fulara, A. A. Awad, J. Åkerman, J. Checiński, and M. Dvornik, Phase-Binarized Spin Hall Nano-Oscillator Arrays: Towards Spin Hall Ising Machines, *Phys. Rev. Appl.* **17**, 014003 (2022).
- [45] C.-F. Pai, L. Liu, Y. Li, H. Tseng, D. Ralph, and R. A. Buhrman, Spin transfer torque devices utilizing the giant spin Hall effect of tungsten, *Appl. Phys. Lett.* **101**, 122404 (2012).
- [46] K. U. Demasius, T. Phung, W. Zhang, B. P. Hughes, S. H. Yang, A. Kellock, W. Han, A. Pushp, and S. S. P. Parkin, Enhanced spin-orbit torques by oxygen incorporation in tungsten films, *Nat. Commun.* **7**, 10644 (2016).
- [47] U. Shashank, R. Medwal, Y. Nakamura, J. R. Mohan, R. Nongjai, A. Kandasami, R. S. Rawat, H. Asada, S. Gupta, and Y. Fukuma, Highly dose dependent damping-like spin-orbit torque efficiency in O-implanted Pt, *Appl. Phys. Lett.* **118**, 252406 (2021).
- [48] M.-H. Nguyen, C.-F. Pai, K. X. Nguyen, D. A. Muller, D. C. Ralph, and R. A. Buhrman, Enhancement of the anti-damping spin torque efficacy of platinum by interface modification, *Appl. Phys. Lett.* **106**, 222402 (2015).
- [49] H. Mazraati, M. Zahedinejad, and J. Åkerman, Improving the magnetodynamical properties of NiFe/Pt bilayers through Hf dusting, *Appl. Phys. Lett.* **113**, 092401 (2018).
- [50] M. Obstbaum, M. Decker, A. K. Greitner, M. Haertinger, T. N. G. Meier, M. Kronseder, K. Chadova, S. Wimmer, D. Ködderitzsch, H. Ebert, and C. H. Back, Tuning Spin Hall Angles by Alloying, *Phys. Rev. Lett.* **117**, 167204 (2016).
- [51] X. Sui, C. Wang, J. Kim, J. Wang, S. H. Rhim, W. Duan, and N. Kioussis, Giant enhancement of the intrinsic spin Hall conductivity in β-tungsten via substitutional doping, *Phys. Rev. B* **96**, 241105 (2017).
- [52] L. Zhu, D. C. Ralph, and R. A. Buhrman, Highly Efficient Spin-Current Generation by the Spin Hall Effect in Au_{1-x}Pt_x, *Phys. Rev. Appl.* **10**, 031001 (2018).

- [53] J.-Y. Kim, D.-S. Han, M. Vafaei, S. Jaiswal, K. Lee, G. Jakob, and M. Kläui, Enhancement of spin Hall conductivity in W-Ta alloy, *Appl. Phys. Lett.* **117**, 142403 (2020).
- [54] L. Qian, K. Wang, Y. Zheng, and G. Xiao, Spin hall effect in the α and β phases of Ta_xW_{1-x} alloys, *Phys. Rev. B* **102**, 094438 (2020).
- [55] C.-F. Pai, Y. Ou, L. H. Vilela-Leão, D. Ralph, and R. Buhrman, Dependence of the efficiency of spin Hall torque on the transparency of Pt/ferromagnetic layer interfaces, *Phys. Rev. B* **92**, 064426 (2015).
- [56] W. Zhang, W. Han, X. Jiang, S.-H. Yang, and S. S. P. Parkin, Role of transparency of platinum–ferromagnet interfaces in determining the intrinsic magnitude of the spin Hall effect, *Nat. Phys.* **11**, 496 (2015).
- [57] See Supplemental Material at <http://link.aps.org/supplemental/10.1103/PhysRevApplied.18.024017>. It contains: X-ray diffraction, frequency dependent STFMR spectra on microbars, Ta concentration dependent effective magnetization and damping, Co-Fe-B thickness dependent sheet conductance, damping like and field like torque efficiencies as a function of Ta composition and Co-Fe-B thickness, threshold current densities estimation of SHNOs, of $W_{100-x}Ta_x(5\text{ nm})/Co\text{-Fe-B}(1.4\text{-}2\text{ nm})/MgO(2\text{ nm})$ stacks, respectively.
- [58] T. Skinner, M. Wang, A. Hindmarch, A. Rushforth, A. Irvine, D. Heiss, H. Kurebayashi, and A. Ferguson, Spin-orbit torque opposing the Oersted torque in ultrathin Co/Pt bilayers, *Appl. Phys. Lett.* **104**, 062401 (2014).
- [59] P. Petroff, T. Sheng, A. Sinha, G. Rozgonyi, and F. Alexander, Microstructure, growth, resistivity, and stresses in thin tungsten films deposited by rf sputtering, *J. Appl. Phys.* **44**, 2545 (1973).
- [60] L. Liu, T. Moriyama, D. C. Ralph, and R. A. Buhrman, Spin-Torque Ferromagnetic Resonance Induced by the Spin Hall Effect, *Phys. Rev. Lett.* **106**, 036601 (2011).
- [61] J. Kim, J. Sinha, M. Hayashi, M. Yamanouchi, S. Fukami, T. Suzuki, S. Mitani, and H. Ohno, Layer thickness dependence of the current-induced effective field vector in $Ta|CoFeB|MgO$, *Nat. Mater.* **12**, 240 (2013).
- [62] Z. Chi, Y.-C. Lau, X. Xu, T. Ohkubo, K. Hono, and M. Hayashi, The spin Hall effect of Bi-Sb alloys driven by thermally excited Dirac-like electrons, *Sci. Adv.* **6**, eaay2324 (2020).
- [63] C. Kim, D. Kim, B. S. Chun, K.-W. Moon, and C. Hwang, Evaluation Method for Fieldlike-Torque Efficiency by Modulation of the Resonance Field, *Phys. Rev. Appl.* **9**, 054035 (2018).
- [64] E. Derunova, Y. Sun, C. Felser, S. Parkin, B. Yan, and M. Ali, Giant intrinsic spin Hall effect in W_3Ta and other A15 superconductors, *Sci. Adv.* **5**, eaav8575 (2019).
- [65] V. Tiberkevich, A. Slavin, and J.-V. Kim, Microwave power generated by a spin-torque oscillator in the presence of noise, *Appl. Phys. Lett.* **91**, 192506 (2007).